Nano Research

ISSN 1998-0124 CN 11-5974/O4
https://doi.org/10.1007/s12274-020-3104-2

Research Article

Confinement and antenna effect for ultrasmall $Y_2O_3:Eu^{3+}$ nanocrystals supported by MOF with enhanced near-UV light absorption thereby enhanced luminescence and excellently multifunctional applications

Hongyi Xu[1], Wenjing Yu[1], Kai Pan[1], Guofeng Wang[1] (✉), and Peifen Zhu[2] (✉)

[1] *Key Laboratory of Functional Inorganic Material Chemistry, Ministry of Education, School of Chemistry and Materials Science, Heilongjiang University, Harbin 150080, China*
[2] *Department of Physics and Engineering Physics, The University of Tulsa, Tulsa, OK 74104, USA*

Received: 9 August 2020 / **Revised**: 7 September 2020 / **Accepted**: 8 September 2020

ABSTRACT

A novel host-guest luminous system with enhanced near-UV light absorption thereby enhanced luminescence are designed based on the synergism of quantum confinement, spatial confinement, and antenna effect, where ultrasmall $Y_2O_3:Eu^{3+}$ nanocrystals are fixed inside MOF (Eu/Y-BTC) as supporting structure. The Eu/Y-BTC not only limits the size and leads to lattice distortion of $Y_2O_3:Eu^{3+}$ nanocrystals and controls the distance between nanocrystals, but also promotes the light absorption and emission. The significantly red-shifted and broadened charge transfer band of $Y_2O_3:Eu^{3+}$/(Eu/Y-BTC) leads to the excellent applications of $Y_2O_3:Eu^{3+}$ in white light-emitting diodes (LEDs). Our results show that white light with superior color quality (CRI>90) and extremely high luminous efficacy (an LER of 335 lm/W) could be achieved using $Y_2O_3:Eu^{3+}$/(Eu/Y-BTC) as red phosphor. The $Y_2O_3:Eu^{3+}$/(Eu/Y-BTC) also improves the photoelectric performance of dye-sensitized solar cells (DSSCs), not only because $Y_2O_3:Eu^{3+}$/(Eu/Y-BTC) has a large specific surface area and the adsorption amount of the dye is increased, but also because the valence band position of $Y_2O_3:Eu^{3+}$/(Eu/Y-BTC) is 2.41 eV, which can provide an additional energy level between the TiO_2 and dye, promoting electron transfer. For these advantageous features, the multifunctional $Y_2O_3:Eu^{3+}$/(Eu/Y-BTC) composite product will open new avenues in white LEDs and DSSCs.

KEYWORDS

confinement effect, antenna effect, enhanced luminescence, ultrasmall $Y_2O_3:Eu^{3+}$ nanocrystals, MOFs, multifunctional applications

1 Introduction

Due to the unique electronic structure, rich energy levels, and characteristic spectral signature of rare-earth ions, the multifunctional rare-earth luminescent materials have the advantages of wide emission spectral range, narrow line-width emission, and stable physical and chemical characteristics, which have made them promising materials to achieve highly efficient optoelectronic devices such as flat displays, solar cell, and new light sources [1–9]. Particularly, rare-earth luminescent materials have very important practical value in advancing solid-state lighting technology. To fully realize the potentials of rare-earth luminescence materials in modern optoelectronic devices, further improving the efficiency of these materials is essential. The cross-section of the absorption band has a significant effect on the emission, which could be increased by engineering charge transfer and confinement. This, in turn, can improve the efficiency of photoelectronic devices [10–14]. At present, rare-earth ions have been successfully introduced into a variety of inorganic metal oxides, inorganic metal salts, and a series of composite products [15–20]. The effects of rare-earth ions on the morphology, luminous properties, and band structure of materials were studied in depth [21–24]. Among them, $Y_2O_3:Eu^{3+}$ exhibits better light emission characteristics and light maintenance characteristics, which has been used in commercial devices [25]. However, the $Y_2O_3:Eu^{3+}$ could not be used in the white light-emitting diodes (LEDs) as it could not efficiently absorb near-UV/blue light. In addition, the size of $Y_2O_3:Eu^{3+}$ synthesized by conventional methods is relatively large, which affects the luminous intensity to some extent. Therefore, synthesizing small-sized $Y_2O_3:Eu^{3+}$ with enhanced near-UV light absorption and solving the agglomeration problem due to lattice defects have become important measures to improve the luminous properties of $Y_2O_3:Eu^{3+}$.

Recently, metal-organic framework (MOF) materials composed of inorganic nodes and organic linkers have attracted extensive attention in photocatalysis [26–29], electrocatalysts [30, 31], single-atom catalysts [32–35], sensing [36–38], and photovoltaic applications [39, 40] due to their superior photoluminescent and electronic properties, and unique pore structure. The rare-earth metal-organic frame (Ln-MOF) has excellent luminous properties due to the rigid skeleton of MOF,

Address correspondence to Guofeng Wang, 2010070@hlju.edu.cn; Peifen Zhu, peifen-zhu@utulsa.edu

rich energy levels of rare metals, and antenna effect [41–47]. MOF has also been used as a precursor to prepare oxide materials [48]. Besides, because of the stable cavity structure and large specific surface area of the MOF and MOF-derived oxides, they also exhibit good properties in terms of dye adsorption [49, 50]. For example, MIL-125 and ZIF-8 have been widely used in the research of photoanodes of dye-sensitized solar cell (DSSC) to improve cell efficiency by increasing the amount of dye adsorbed and inhibiting charge recombination [51]. More importantly, MOF is also an excellent platform for host-guest chemistry. The composite materials composed of two or more materials can have the properties of all single materials [52]. In addition, the spatial confinement effect can effectively improve the properties of materials, and thus, they may have a wide range of applications and more novel properties [53]. However, Y_2O_3:Eu^{3+}/Ln-MOF host-guest nanocomposites have never been reported because the size of Y_2O_3:Eu^{3+} prepared by traditional methods is too large to fit into MOF matrices.

Based on the consideration of the quantum and spatial confinement effect of ultrasmall Y_2O_3:Eu^{3+} as well as the antenna effect of Ln-MOF, we propose a new composite luminescence system with enhanced near-UV light absorption thereby enhanced luminescence, where ultrasmall Y_2O_3:Eu^{3+} nanocrystals with larger specific surface areas were fixed inside Eu/Y-BTC as supporting structure (Scheme 1). As we expected, enhanced luminescence was observed from Y_2O_3:Eu^{3+} by using MOF (Eu/Y-BTC) as a supporting structure, because the Eu/Y-BTC can promote the absorption of light as well as changing the local symmetry around Eu^{3+} ions. Both the excitation band and emission peaks of Y_2O_3:Eu^{3+}/(Eu/Y-BTC) show broadened compared to Y_2O_3:Eu^{3+}. There is also a redshift for the excitation band as well as a red shift for the emission peaks of Y_2O_3:Eu^{3+}/(Eu/Y-BTC) compared to that of Y_2O_3:Eu^{3+}, which could overcome the shortcomings of weak absorption of near UV light for Y_2O_3:Eu^{3+} and lead to potential applications in highly efficient and high-quality white LEDs [54–56]. The specific surface areas of Y_2O_3:Eu^{3+}/(Eu/Y-BTC) was calculated to be 118.4779 m^2/g, which is conducive to the adsorption of dyes, thus improving the efficiency of the cells. More importantly, the valence band positions of Y_2O_3:Eu^{3+}/(Eu/Y-BTC) are calculated to be 2.41 eV, which can provide an additional energy level between the TiO_2 and dye, promoting efficient electron transfer [57].

2 Results and discussion

2.1 Design scheme of overall work

As mentioned above, Y_2O_3:Eu^{3+} as a highly efficient red phosphor has been used in fluorescent lamps for decades as it can absorb 254-nm light and emit bright red light. However, this material has not been used in white LEDs due to the weak absorption of near UV light. To solve this problem, a new composite luminescence system with enhanced near-UV light absorption thereby enhanced luminescence was proposed based on the quantum and spatial confinement effect of ultrasmall Y_2O_3:Eu^{3+} as well as the antenna effect of Eu/Y-BTC, as shown in Scheme 1. The molecular structure of Ln-BTC is shown in Fig. S1 in the Electronic Supplementary Material (ESM).

As we expected, Eu/Y-BTC was prepared by the solvothermal method under moderate conditions first, and then the transformation of Eu/Y-BTC into Y_2O_3:Eu^{3+}/Eu/Y-BTC and Y_2O_3:Eu^{3+} was achieved by calcination of Eu/Y-BTC at different temperatures. A series of characterization results show that many ultrasmall Y_2O_3:Eu^{3+} nanocrystals with larger specific surface areas were fixed inside Eu/Y-BTC as supporting structure, which will be proved in detail later. More importantly, the Eu/Y-BTC remains a framework structure for Y_2O_3:Eu^{3+}/Eu/Y-BTC, and thus, the Eu/Y-BTC not only limits the size and leads to lattice distortion of ultrasmall Y_2O_3:Eu^{3+} nanocrystals as well as controls the distance between nanocrystals during the synthesis process, but also promotes the light absorption and emission as well as changing the value of J-O parameters, which directly affects the intensity of $^5D_0 \rightarrow {}^7F_2$ emission of Eu^{3+} ions.

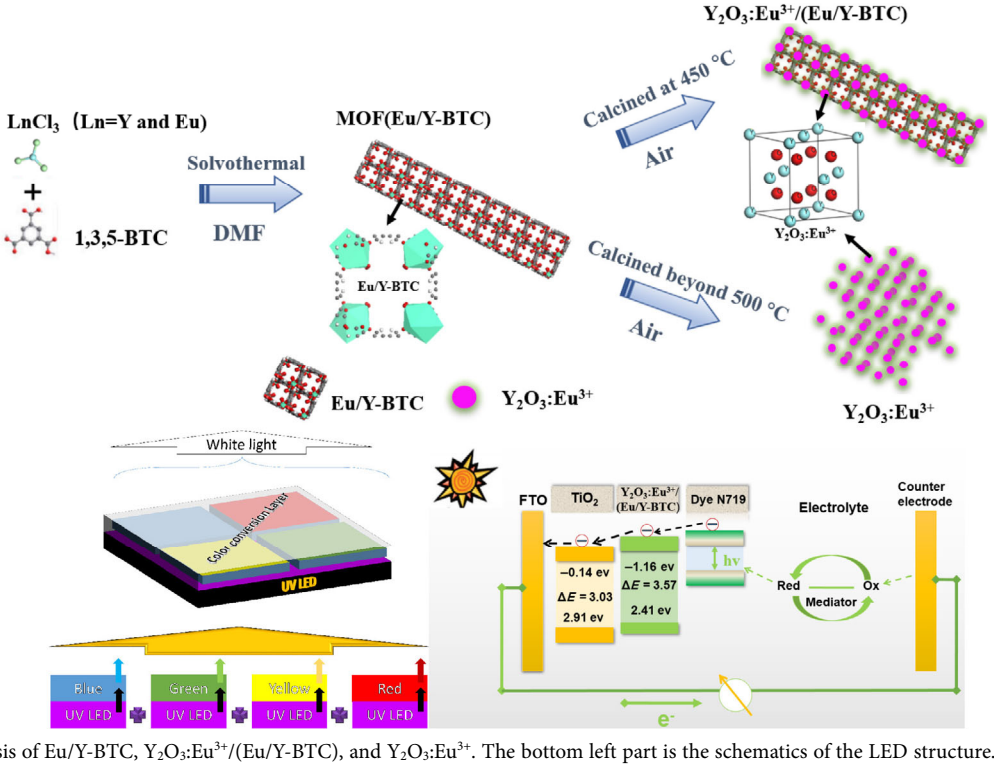

Scheme 1 Synthesis of Eu/Y-BTC, Y_2O_3:Eu^{3+}/(Eu/Y-BTC), and Y_2O_3:Eu^{3+}. The bottom left part is the schematics of the LED structure. The bottom right part is the schematics of the working principle of TiO_2-Y_2O_3:Eu^{3+}/(Eu/Y-BTC) composite cells.

The bottom left part is the designed LED application process, and the red-emitting Y_2O_3:Eu^{3+}/(Eu/Y-BTC) was combined with blue, green, and yellow-emitting perovskites to obtain the white LEDs. The bottom right part is the schematic working principle of TiO_2-Y_2O_3:Eu^{3+}/(Eu/Y-BTC) composite cells. An intermediate energy level was formed by inserting Y_2O_3:Eu^{3+}/(Eu/Y-BTC) between TiO_2 and dye, which leads to reduced electron loss and the reduced charge recombination. The energy level formed by Y_2O_3:Eu^{3+}/Eu/Y-BTC makes the photo-generated electrons easier to be transported from dye to TiO_2 instead of recombining with holes in the valence band, which leads to effective electron-hole separation.

2.2 Morphology and structure analysis

The powder X-ray diffraction (P-XRD) patterns of the MOFs prepared by the solvothermal method are shown in Fig. 1(a). According to different kinds of rare-earth ions, the MOFs without calcination are marked as Y-BTC and Eu/Y-BTC, respectively. The characteristic diffraction peaks of Y-BTC and Eu/Y-BTC are nearly identical to literature ones of $Eu(BTC)(H_2O)\cdot 1.5H_2O$ (CCDC-617492(1)) [58]. It is thus confirmed that the crystal lattice of as-prepared MOFs is identical to that of $Eu(BTC)(H_2O)\cdot 1.5H_2O$, and belongs to the tetragonal space group *P*4(3)22.

The P-XRD patterns of Eu/Y-BTC at different calcination temperatures are shown in Fig. 1(b), which is consistent with results from TGA measurements discussed later. When the calcination temperature is 400 °C, the sample maintains characteristic XRD peaks of Eu/Y-BTC. However, when the calcination temperature is 450 °C, the samples become the composite-product Y_2O_3:Eu^{3+}/(Eu/Y-BTC), where ultrasmall Y_2O_3:Eu^{3+} nanoparticles are confined within the Eu/Y-BTC framework structure. When the temperature is 500 °C, the main component is Y_2O_3:Eu^{3+} nanocrystals. When the temperature increases to 550 °C, the characteristic diffraction peaks of Eu/Y-BTC disappear completely, indicating that Eu/Y-BTC was completed transformed into Y_2O_3:Eu^{3+}. The TGA measurement of Eu/Y-BTC was performed under an ambient atmosphere and the results are shown in Fig. 1(c). The weight loss at the temperature range between 25 °C and 150 °C is mainly due to the release of free and terminal water molecules from Eu/Y-BTC, and the weight loss around 350 °C is attributed to the degradation of the free-BTC ligand. When the temperature is higher than 430 °C, the weight loss is attributed to the gradual loss of ligands. When the temperature reaches 520 °C, the weight loss is attributed to the collapse of the organic framework completely, and stable oxides are formed. Therefore, Y_2O_3:Eu^{3+}/(Eu/Y-BTC) composite materials can be obtained by choosing the appropriate calcination temperature, and the transmission electron microscopy (TEM) images discussed later will further demonstrate the confinement effects and lattice distortion of ultrasmall Y_2O_3:Eu^{3+} nanocrystals inside Eu/Y-BTC.

The Fourier transform infrared (FT-IR) spectra of Eu/Y-BTC and Eu/Y-BTC sintered at different temperatures are shown in Fig. 1(d). The Eu/Y-BTC calcined at 400 °C still has typical peaks of organic linkers. The characteristic absorption bands at 1,538–1,575 and 1,383–1,442 cm^{-1} are attributed to the asymmetry and symmetric stretching vibrations of –COO–, respectively. This is a typical characteristic peak of metal-organic framework material (MOF) [59]. After the sample is calcined at high temperature, there are still characteristic peaks of –COO– and C=O in the spectrum, which proves that the calcined product contains trace amounts of MOF. Among them, the characteristic bands near 1,635 cm^{-1} in the samples of Eu/Y-BTC and Eu/Y-BTC(400 °C) can be attributed to the uncoordinated –COOH group. The absorption peaks of Y_2O_3:Eu^{3+} (500 °C) and Y_2O_3:Eu^{3+}/(Eu/Y-BTC) (450 °C) at 1,524 cm^{-1} and 1,402 cm^{-1} are attributed to the stretching vibration of the C–O bond. The band centered at 771 cm^{-1} may be designated as a ring-out of plane deformation vibration of the benzene nucleus of the substituted 1,3,5-benzenetricarboxylic acid. The small bands around 460 and 567 cm^{-1} are from the Y-O interaction, demonstrating that the Y atoms have successfully coordinated to the carboxyl groups. The broadband around 3,500 cm^{-1} corresponds to the absorption peak of –OH group in water molecules. When the calcination temperature exceeds 450 °C, the sample gradually becomes Y_2O_3:Eu^{3+} and the characteristic peaks of the organic linkers disappear.

The UV–vis absorption spectra of Eu/Y-BTC and the samples at different calcination temperatures were recorded in the solid state at room temperature. As shown in Fig. 1(e), Eu/Y-BTC has a strong absorption band around 286 nm. The

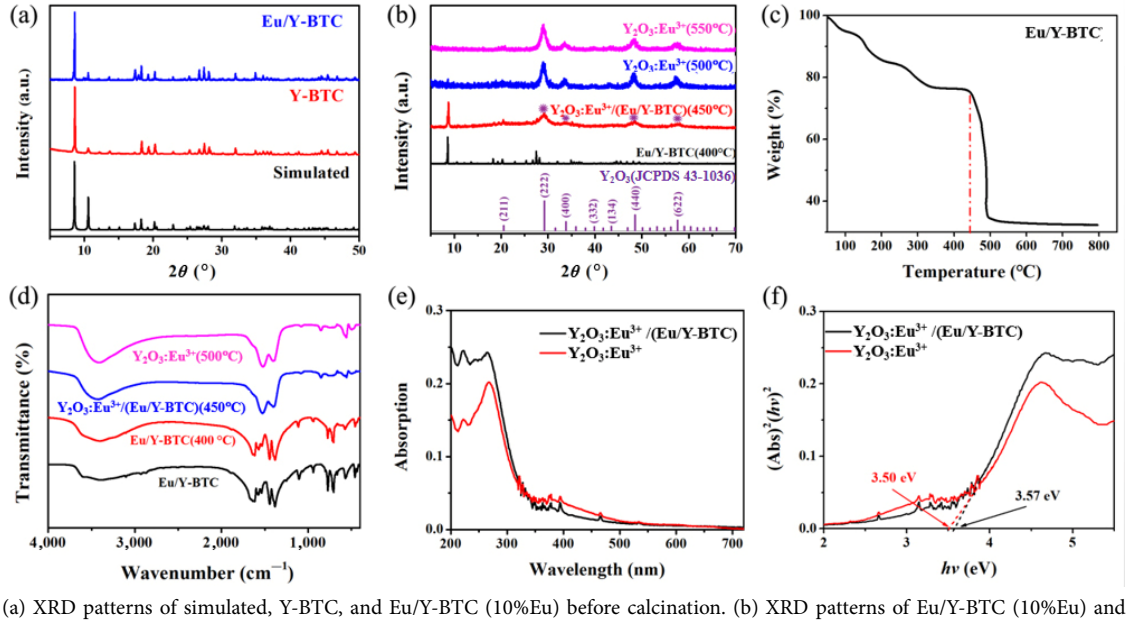

Figure 1 (a) XRD patterns of simulated, Y-BTC, and Eu/Y-BTC (10%Eu) before calcination. (b) XRD patterns of Eu/Y-BTC (10%Eu) and Eu/Y-BTC (10%Eu) sintered at different temperatures. (c) TGA curve of Eu/Y-BTC (10%Eu). (d) FT-IR spectra of Eu/Y-BTC (10%Eu) sintered at different temperatures. (e) UV–vis absorption spectra of Y_2O_3:Eu^{3+}/(Eu/Y-BTC) and Y_2O_3:Eu^{3+}. (f) The bandgap of Y_2O_3:Eu^{3+}/(Eu/Y-BTC) and Y_2O_3:Eu^{3+}.

weak absorption peaks at longer wavelengths are mainly attributed to the absorption of Eu^{3+} ions. Theoretically, the multiple absorption bands of benzene centered at 254 nm should be produced due to the overlap of the π→π* type transition and the vibrational level transition of the aromatic ring. After coordination of rare-earth ions, the orbital energy of π* is decreased due to the conjugated interaction between the π→π* and n→π* transitions of the C=O group [60]. Thus, the energy required for the π→π* and n→π* transitions is lowered, and the absorption band of Eu/Y-BTC is red-shifted than that of H_3BTC ligands before the coordination of rare-earth ions. Furthermore, when Y^{3+}/Eu^{3+} ions are coordinated with the benzoylformic acid, the charge density on the oxygen atom and the conjugate effect increase, and the absorption peak is red-shifted. More importantly, the results showed that the absorption peaks of Y_2O_3:Eu^{3+}/(Eu/Y-BTC) is enhanced than those of Y_2O_3:Eu^{3+}, which is in a good agreement with results from the excitation spectra discussed later. Figure 1(f) shows the bandgap of Y_2O_3:Eu^{3+} is narrower compared to that of Y_2O_3:Eu^{3+}/(Eu/Y-BTC), indicating that Y_2O_3:Eu^{3+} can broaden the photoelectric response area and improve the utilization of light, which will improve the performance of LEDs and DSSCs. The composite materials Y_2O_3:Eu^{3+}/(Eu/Y-BTC) mentioned in the article are all prepared at 450 °C with Eu/Y-BTC as the precursor, and the Y_2O_3:Eu^{3+} mentioned are all prepared at 500 °C with Eu/Y-BTC as the precursor.

The TEM measurements were carried out to further prove the confinement of ultrasmall Y_2O_3:Eu^{3+} nanocrystals inside MOF. The TEM images in Figs. 2(a)–2(c) show that the prepared Eu/Y-BTC without calcination and Eu/Y-BTC sintered at 400 °C are a large-sized micron rod-like structure with a smooth and continuous surface. The TEM images of Eu/Y-BTC (30%Eu) are shown in Fig. S2 in the ESM. When Eu/Y-BTC is calcined at a high temperature in the ambient atmosphere, the carbon in the skeleton gradually loses and changes significantly in a shorter temperature range, and thus, it produces metal oxides and carbon dioxide. As shown in Fig. 2, when the calcination temperature rises to 450 °C, there are intermediate pores on the surface and inside of the sample, and the composite-product Y_2O_3:Eu^{3+}/(Eu/Y-BTC) still maintains the skeletal morphology due to the support of Eu/Y-BTC, proving the space confinement of ultrasmall Y_2O_3:Eu^{3+} nanocrystals inside MOF. When the temperature was raised to 500 °C, most of the Eu/Y-BTC structure collapsed, and the small particles of Y_2O_3:Eu^{3+} with a mean size of 6 nm were obtained. The HRTEM images in Fig. 2(f) show that the lattice spacing of Y_2O_3:Eu^{3+}/(Eu/Y-BTC) composite is 0.295 nm, which corresponds to the Y_2O_3:Eu^{3+} (222) crystal plane. While the lattice spacing for (222) crystal plane of Y_2O_3:Eu^{3+} small particles prepared by using MOF as a precursor is 0.305 nm at the sintering temperature of 500 °C as shown in Fig. 2(h). We speculate that the reason for the inconsistent lattice spacing is lattice distortion.

The X-ray photoelectron spectroscopy (XPS) spectra of the Eu/Y-BTC at different calcination temperatures are presented in Fig. 3(a). The signals contained in the XPS spectra can be attributed to the electronic transitions of Y, Eu, C, and O. By comparing the XPS spectra of samples calcined at different temperatures, it can be obtained that the peaks of Eu and Y gradually become apparent with increasing the calcination temperature, and the peak of C gradually decreases. The measurement was carried out on the surface of the sample. We speculated that the Eu/Y-BTC without calcination contained a large amount of organic framework, and only a small amount of metal was exposed on the surface, and thus the peaks of Eu and Y in the spectra are not obvious. As the calcination temperature increases, the sample is oxidized in the air and the C in the sample is gradually lost. All these are consistent with the XRD results discussed above. Furthermore, Eu^{3+} is identified by Eu 3d and Eu 4d peaks, and the Y 3s, Y3p, Y3d, and Y 4p peaks indicate the presence of Y^{3+}. The Eu 4d scan is presented in Fig. 3(b), and the peaks located at ~135.10 eV and ~140.84 eV produced by fitting are attributed to Eu $4d_{5/2}$ and Eu $4d_{3/2}$, respectively. The Y 3d scan is shown in Figure 3(c), and peaks located at ~ 155.97, ~ 157.82, and ~ 159.75 eV obtained by fitting are ascribed to Y $3d_{5/2}$ and Y $3d_{3/2}$, respectively. The peaks at ~284.46, ~ 285.85, ~ 287.53, and ~ 289.38 eV shown in Fig. 3(d) belong to C 1s. The peaks at ~ 528.94, ~ 531.51, and ~ 532.29 eV in Fig. 3(e) originated from O 1s. The valence band edge positions of Eu/Y-BTC (10%Eu) and Y_2O_3:Eu^{3+}/(Eu/Y-BTC) (10%Eu, 450 °C) are calculated to be 2.68 and 2.41 eV, respectively. Figures S3–S5 in the ESM is the XPS spectra of the Eu/Y-BTC (10%Eu) without calcination and Eu/Y-BTC (10%Eu) sintered at different temperatures. We found that compared with Eu/Y-BTC, the binding energy of Eu 4d in Y_2O_3:Eu^{3+}/(Eu/Y-BTC) (450 °C) has a negative shift (1.61 eV). This is due to the formation of Ln_2O_3, which results

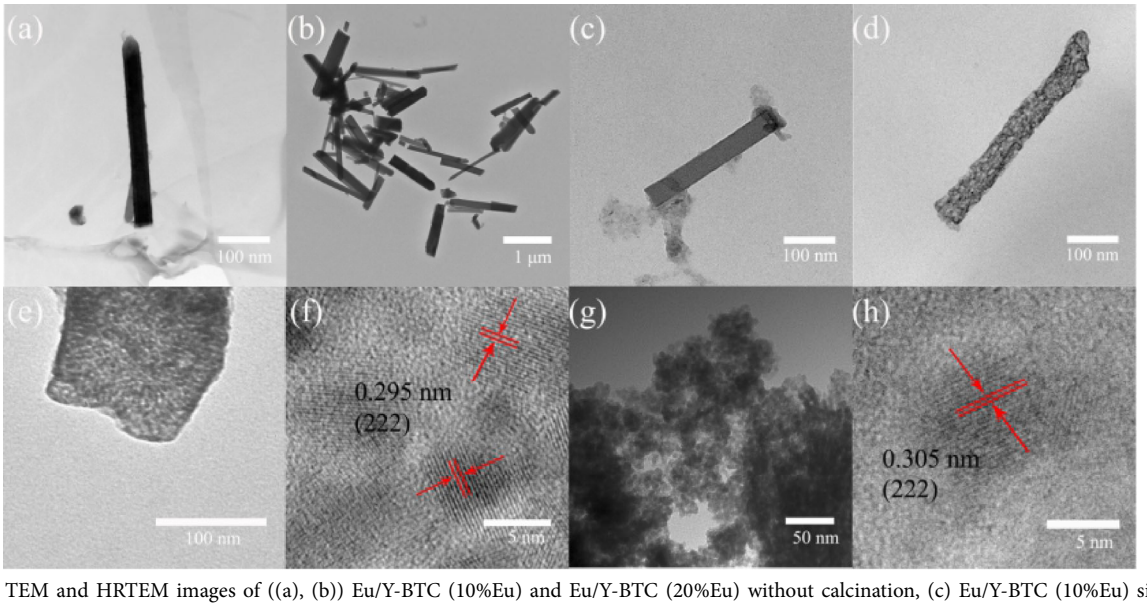

Figure 2 TEM and HRTEM images of ((a), (b)) Eu/Y-BTC (10%Eu) and Eu/Y-BTC (20%Eu) without calcination, (c) Eu/Y-BTC (10%Eu) sintered at 400 °C. (d)–(f) Y_2O_3:Eu^{3+}/(Eu/Y-BTC), and ((g), (h)) Y_2O_3:Eu^{3+}.

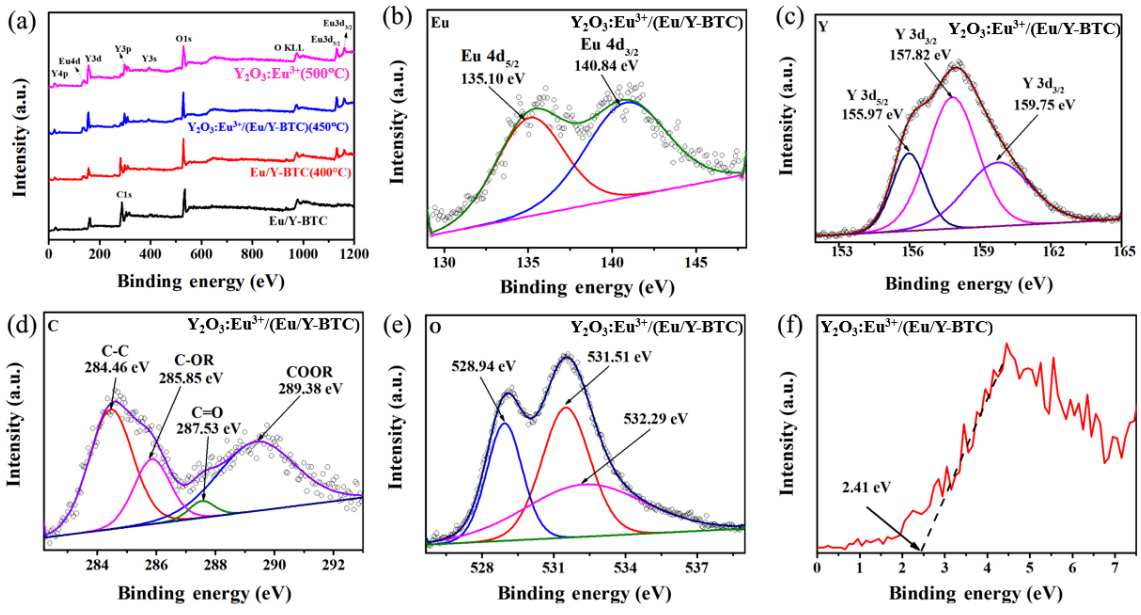

Figure 3 (a) The survey XPS spectra of Eu/Y-BTC (10%Eu) sintered at different temperatures. (b)–(e) High-resolution XPS spectra of Eu, Y, C, O in Y_2O_3:Eu^{3+}/(Eu/Y-BTC) (10%Eu). (f) XPS valence-band spectrum of Y_2O_3:Eu^{3+}/(Eu/Y-BTC) (10%Eu).

in strong interaction between the nanocrystals. Thus, ultrasmall Y_2O_3:Eu^{3+} guest nanocrystals are confined inside the Eu/Y-BTC host material. The N_2 adsorption–desorption isotherms and BJH pore size distribution plots of samples with different calcination temperatures are shown in Fig. S6 in the ESM. The N_2 adsorption–desorption isotherm curve of Eu/Y-BTC (400 °C) belongs to type I, and the hysteresis loop belongs to type H4. These indicate that the sample has more micropores and slit holes are formed by the layered structure. The N_2 adsorption-desorption isotherm curve of Y_2O_3:Eu^{3+}/(Eu/Y-BTC) (450 °C) belongs to type IV, and the hysteresis loop belongs to type H3 caused by the aggregation of the capillary and the aggregation of the particles in the structure, indicating that the sample has typical mesoporous structure. All this further proves the confinement of ultrasmall Y_2O_3:Eu^{3+} nanocrystals supported by Eu/Y-BTC.

The specific surface areas of Eu/Y-BTC (400 °C) and Y_2O_3:Eu^{3+}/(Eu/Y-BTC) (450 °C) calculated by BET theory are 846.9277 and 118.4779 m^2/g, respectively. The desorption average pore width of Eu/Y-BTC (400 °C) and Y_2O_3:Eu^{3+}/(Eu/Y-BTC) (450 °C) were 4.6925 nm and 17.4622 nm, respectively. Compared with Eu/Y-BTC, the decrease of the specific surface areas as well as the increase of the pore widths of Y_2O_3:Eu^{3+}/(Eu/Y-BTC) can be attributed to the formation of the intermediate pores on the surface and inside of the sample, and the frame structure is on the verge of collapse. By discussing the existing data, Y_2O_3:Eu^{3+}/(Eu/Y-BTC) still retains a certain skeleton structure. Note that the specific surface area of Y_2O_3:Eu^{3+} supported by Eu/Y-BTC is larger than that of Y_2O_3:Eu^{3+} prepared by the conventional method. The larger specific surface area has positive effects on both dye adsorption and luminescence properties.

2.3 Luminescence properties

We investigated the effects of spatial confinement and rare-earth doping concentration on luminescent properties. The excitation spectra of Y_2O_3:Eu^{3+}/(Eu/Y-BTC) and Y_2O_3:Eu^{3+} monitored at 618-nm emission are shown in Fig. 4(a). The excitation spectra of Eu/Y-BTC and Eu/Y-BTC sintered at 400 °C by monitoring 618-nm emission are also presented in Fig. S7 in the ESM for the comparison purpose. The strong spectral band around 300 nm is mainly from the multiple absorption bands of benzene due to the overlap of the π-π* type transition and the vibrational level transition of the aromatic ring. In addition, the charge transfer transitions from the 2p orbital of O^{2-} to the 4f orbital of Eu^{3+} as well as the n→π* transitions of the C=O group also play an important role in the excitation spectra. These ligands in the MOFs sensitize Ln^{3+} and increase its luminescence intensity, which is the so-called antenna effect. The sharp excitation peaks are caused by the f-f transition of Eu ions. Compared with Y_2O_3:Eu^{3+}, the excitation peak intensity of Y_2O_3:Eu^{3+}/(Eu/Y-BTC) increases obviously. The position of the excitation band of Y_2O_3:Eu^{3+}/(Eu/Y-BTC) undergoes a red-shift and broadening compared to that of Y_2O_3:Eu^{3+}, which can be attributed to the quantum confinement effect of ultrasmall Y_2O_3:Eu^{3+} particles inside Y_2O_3:Eu^{3+}/(Eu/Y-BTC). All of these will be discussed in detail later.

Compared with Y_2O_3:Eu^{3+}, not only the emission peak intensity of Y_2O_3:Eu^{3+}/(Eu/Y-BTC) increases, but also the emission peaks of Eu/Y-BTC and Y_2O_3:Eu^{3+}/(Eu/Y-BTC) show a red-shift and broadening. The emission peaks of Y_2O_3:Eu^{3+}/(Eu/Y-BTC) and Y_2O_3:Eu^{3+} split compared with those of Eu/Y-BTC and Eu/Y-BTC sintered at 400 °C. We speculate that the intensity of the peak is not only affected by the crystallinity and size of the Y_2O_3:Eu^{3+} but also affected by the spatial confinement and antenna effect of Eu/Y-BTC. Figure 4(c) shows the excitation spectra of Y_2O_3:Eu^{3+}/(Eu/Y-BTC) composite-product with different Eu^{3+} contents, which was monitored at 618-nm emission.

Figure 4(d) shows the emission spectra of Y_2O_3:Eu^{3+}/(Eu/Y-BTC) with different Eu^{3+} contents, which was excited by 296-nm light. It was found that Y_2O_3:Eu^{3+}/(Eu/Y-BTC) has both Y_2O_3:Eu^{3+} and Eu/Y-BTC down-converted fluorescence characteristic peaks. As the concentration increases, the luminous intensity also increases first and then decreases. When the doping concentration is 10%, the light emission intensity is the strongest. At the same time, we measured the excitation spectra of Y_2O_3:Eu^{3+}/(Eu/Y-BTC) composite-products by monitoring the different emission wavelengths and the emission spectra of those at different excitation wavelengths. Figure 4(e) is the excitation spectra of Y_2O_3:Eu^{3+}/(Eu/Y-BTC) at different detection wavelengths. When the detection wavelength is 618 nm, its excitation spectrum intensity is the highest. Figure 4(f) is the

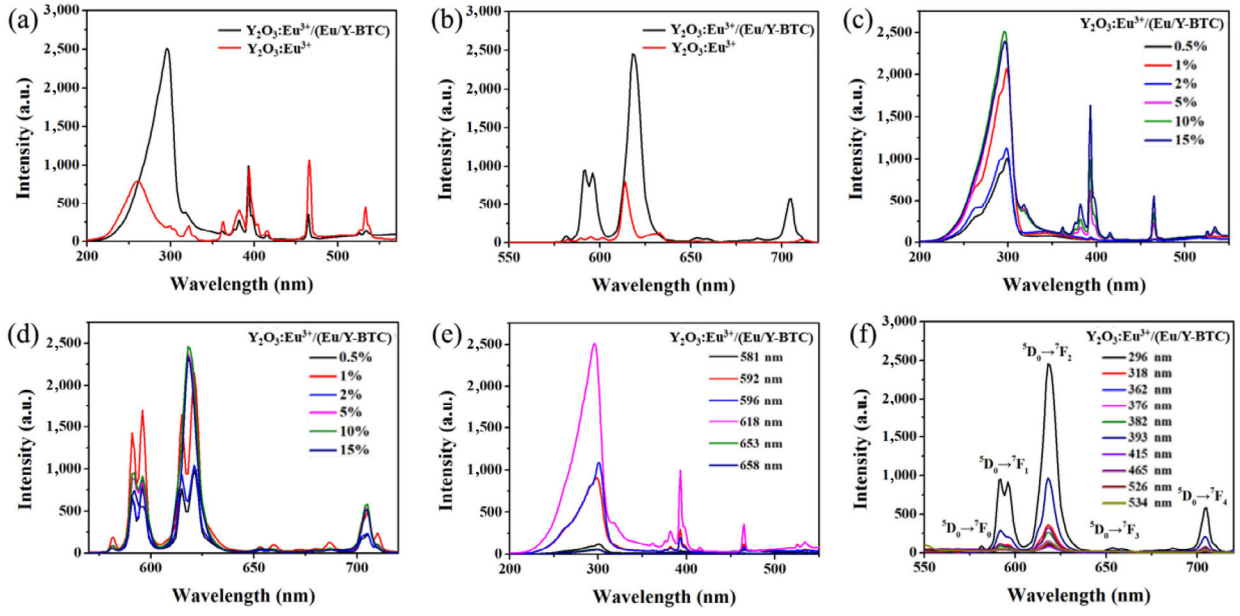

Figure 4 (a) Excitation spectra of Y_2O_3:Eu^{3+}/(Eu/Y-BTC) and Y_2O_3:Eu^{3+} monitored at 618 nm. (b) Emission spectra of Y_2O_3:Eu^{3+}/(Eu/Y-BTC) and Y_2O_3:Eu^{3+} excited at 296 nm. (c) Excitation spectra of Y_2O_3:Eu^{3+}/(Eu/Y-BTC) with different Eu^{3+} concentrations monitored at 618 nm. (d) Emission spectra of Y_2O_3:Eu^{3+}/(Eu/Y-BTC) with different Eu^{3+} concentrations excited at 296 nm. (e) Excitation spectra of Y_2O_3:Eu^{3+}/(Eu/Y-BTC) (10%Eu) monitored at different wavelengths. (f) Emission spectra of Y_2O_3:Eu^{3+}/(Eu/Y-BTC) (10%Eu) excited at different wavelengths.

emission spectrum of Y_2O_3:Eu^{3+}/(Eu/Y-BTC) under different wavelength light excitation. When the excitation wavelength is 296 nm, its emission spectrum intensity is the highest, however, the peak position does not change. Figure S8(a) in the ESM presents the excitation spectra of Y_2O_3:Eu^{3+} with different Eu^{3+} contents, which was monitored at 618-nm emission. Figure S8(b) in the ESM is the emission spectra of Y_2O_3:Eu^{3+} with different Eu^{3+} contents excited at 296 nm. When the doping concentration is 2%, the light emission intensity is the strongest.

In addition, we calculated the J-O parameters of different samples from emission spectra, and the results are summarized in Table 1. Generally, the change of the values of Ω_4 are smaller than those of Ω_2, and thus, the values of Ω_2 are related to the symmetry around Eu^{3+} ions, which directly affects the intensity of $^5D_0 \rightarrow {}^7F_2$ emission peak. When the Eu^{3+} concentration is fixed at 10 mol%, the values of Ω_2 are calculated to be 4.99×10^{-20}, 6.01×10^{-20}, 4.49×10^{-20}, and 1.14×10^{-20} cm^2 for Eu/Y-BTC, Eu/Y-BTC sintered at 400 °C, Y_2O_3:Eu^{3+}/(Eu/Y-BTC), and Y_2O_3:Eu^{3+}, respectively. In addition, the values of Ω_2 of Y_2O_3:Eu^{3+}/(Eu/Y-BTC) increase with increasing Eu^{3+} concentrations. This is attributed to the energy transfer from the Eu^{3+} at C_{3i} to that at C_2 sites. The transitions of Eu^{3+} are sensitive to the crystal field environment and this results in different optical properties of Eu^{3+} at different symmetry sites. The intra-configurational f-f electric dipole transitions took place for the Eu^{3+} located in noncentrosymmetric sites (C_2) and have high intensity, which is more favorable. The magnetic dipoles transition for the Eu^{3+} in centrosymmetric sites (C_{3i}) has low efficiency which is not favorable for practical applications. The energy transfer from the Eu^{3+} at C_{3i} to that at C_2 sites increases with the increase in the Eu^{3+} concentration. Thus, the ratio of electric dipole transition to magnetic dipole transition increases with concentration and leads to the significantly enhanced emission, which is reflected in the increase of Ω_2. The change of the Ω_2 values show that the local symmetry around Eu^{3+} ions has changed, which was caused by the synergism of the quantum confinement effect of Y_2O_3:Eu^{3+} and the spatial confinement effect as well as the antenna effect of Eu/Y-BTC.

To further study the quantum confinement effect and space confinement effect on the enhanced near-UV light absorption thereby enhanced luminescence, the excitation bands of samples in the range of 220–350 nm were fitted with five or eight Gaussian curves, respectively. The excitation bands of Eu/Y-BTC, Eu/Y-BTC sintered at 400 °C, and Y_2O_3:Eu^{3+}/(Eu/Y-BTC) can be fitted with five Gaussian curves, while the excitation band of Y_2O_3:Eu^{3+} can be fitted with eight Gaussian curves. Since Y_2O_3 in the Y_2O_3:Eu^{3+}/(Eu/Y-BTC) structure is small in size, there is a quantum confinement effect, but this factor has a little influence on the luminous intensity. The strong and broad excitation peaks of Eu/Y-BTC overlaps with the excitation peak of Y_2O_3:Eu^{3+}, so the Gaussian curves of Y_2O_3:Eu^{3+}/(Eu/Y-BTC) will decrease. For Eu/Y-BTC, Eu/Y-BTC sintered at 400 °C, and Y_2O_3:Eu^{3+}/(Eu/Y-BTC), the first peak at 256 nm is attributed to the CTB $Eu^{3+} \rightarrow O^{2-}$, and the other four peaks are attributed

Table 1 The calculated J-O parameters and the emission peak area ratios of $^5D_0$-$^7F_2$/$^5D_0$-$^7F_1$ from the emission spectra of different samples (Fig. 5)

Samples	Ω_2 ($\times 10^{-20}$ cm^2)	Ω_4 ($\times 10^{-20}$ cm^2)	Peak area ratios $^5D_0$-$^7F_2$/$^5D_0$-$^7F_1$
Eu/Y-BTC (10%Eu)	4.99	2.01	2.66
Eu/Y-BTC (10%Eu, 400 °C)	6.01	2.05	3.14
Y_2O_3:Eu^{3+}/(Eu/Y-BTC) (0.5%Eu)	2.70	1.32	1.69
Y_2O_3:Eu^{3+}/(Eu/Y-BTC) (2%Eu)	3.00	1.38	1.86
Y_2O_3:Eu^{3+}/(Eu/Y-BTC) (10%Eu)	4.49	1.84	2.68
Y_2O_3:Eu^{3+}/(Eu/Y-BTC) (15%Eu)	5.31	2.15	3.14
Y_2O_3:Eu^{3+} (10%Eu)	1.14	1.40	3.76

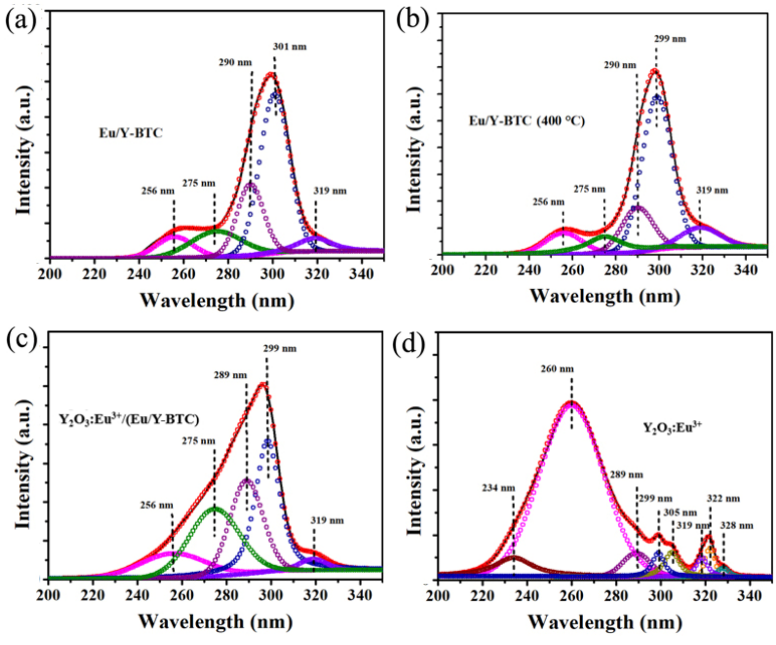

Figure 5 The excitation bands of (a) Eu/Y-BTC, (b) Eu/Y-BTC sintered at 400 °C, (c) Y_2O_3:Eu^{3+}/(Eu/Y-BTC), and (d) Y_2O_3:Eu^{3+} in the range of 220–350 nm can be fitted with five and eight Gaussian curves, respectively.

to the multiple absorption bands of ligands. Due to the change of coordination environment around Eu^{3+} caused by calcination, the positions of these excitation peaks are slightly shifted. The CTB (Eu^{3+}→O^{2-}) of Y_2O_3:Eu^{3+}/(Eu/Y-BTC) is wider than that of Eu/Y-BTC, while narrower than that of pure Y_2O_3:Eu^{3+}. Furthermore, the three narrow excitation peaks at 305, 322, and 328 nm for Y_2O_3:Eu^{3+} are attributed to the f-f transition of Eu ions, and the excitation band at 234 nm is attributed to the absorption of Y_2O_3. In addition, the CTB Eu^{3+}→O^{2-} of Y_2O_3:Eu^{3+}/(Eu/Y-BTC) shows blue-shift compared to Y_2O_3:Eu^{3+}, indicating that the particle size of Y_2O_3:Eu^{3+} inside Y_2O_3:Eu^{3+}/(Eu/Y-BTC) is smaller than that of pure Y_2O_3:Eu^{3+}.

2.4 Potential applications in white LEDs

The significantly red-shifted charge transfer band of Y_2O_3:Eu^{3+}/(Eu/Y-BTC) obtained in this work compared to that of Y_2O_3:Eu^{3+} reported in the literature might open new application avenues. The Y_2O_3:Eu^{3+} as an economic and highly efficient red phosphor has been used in fluorescent lamps, field emission displays, and projection television for many decades. As mentioned above, the traditional Y_2O_3:Eu^{3+} could not be used in the white LED applications as it could not efficiently absorb near-UV/blue light and emit red light. In this work, we have shifted the charge transfer band from ~ 250 nm to ~ 300 nm. Thus, they can absorb near near-UV light from III-nitride LEDs to emit red light. In this work the red-emitting Y_2O_3:Eu^{3+}/(Eu/Y-BTC) was combined with blue, green, and yellow–emitting perovskites to obtain the white LEDs.

We performed extensive calculations to optimize the white LED device structure. Specifically, white LED spectra were optimized by tuning the ratios of different emissions. Then color characteristics of these LED spectra were calculated with the goal of finding the best combinations and the fundamental limit. The results show that the white light with extremely high color rendering index (>90), high luminous efficacy (up to 335 lm/W) could be achieved by choosing the suitable ratios of different emission. The color temperature of white light could also be tuned by simply adjusting the ratios of materials used in the fabrication of white LEDs. The color characteristics of 6 representative white LED with various CCT are summarized in Table S1 in the ESM. Note that the ratios listed in Table S1 in the ESM were normalized by using the blue emission. A CCT of 4,992 of white light was obtained at power ratios of 1:1.15:0.95:1.27, and the corresponding LER is 335 lm/W, which is the highest LER obtained among all the combinations. White light with the CIE coordinates of (0.323, 0.333) and the CCT of 5,933 K was obtained by slightly decreasing green, yellow, and red emission. The continuous increase of CCT and CAF was obtained by keeping decreasing the amount of green, yellow, and red-emitting materials used in the fabrication of white LEDs. The spectral power distributions of these LEDs are plotted in Fig. 6(a) and CIE coordinates are shown in

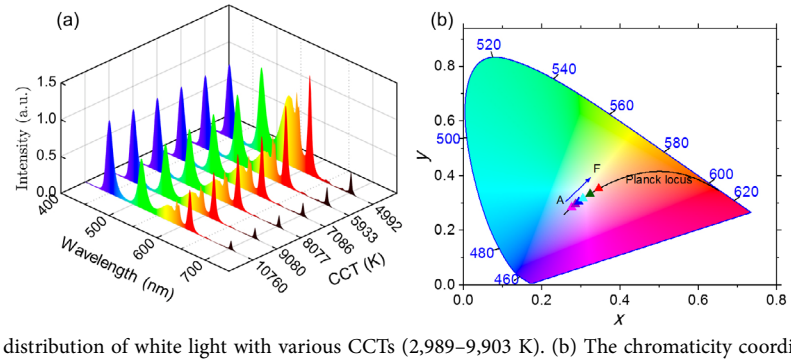

Figure 6 (a) Spectral power distribution of white light with various CCTs (2,989–9,903 K). (b) The chromaticity coordinates of white light in the CIE 1931 chromaticity diagram.

Fig. 6(b). No obvious deviation from Planck locus is observed, indicating the extremely small D_{uv} and the pure white light was obtained.

To provide guidelines for the fabrication of white LEDs with high color quality, tunable CCT, and excellent vision performance by using metal halide perovskites and Y_2O_3:Eu^{3+}/(Eu/Y-BTC) composites, we investigated the color characteristics of white light on various parameters and we found that ratio of the amount of blue and green-emitting materials to that of yellow and red-emitting materials determine the CCT, CAF, and LER. As shown in Figs. 7(a), 7(c), and 7(e), both the CCT and CAF increase with the ratio, however, LER decreases with the ratio. Higher LER and lower CCT could be obtained at a smaller ratio, while higher CCT and lower LER could be obtained at a larger ratio. In general, by incorporating more Y_2O_3:Eu^{3+}/(Eu/Y-BTC) into white LEDs, the LER could be increased as shown in Fig. 7(d), in the meantime, the CCT and CAF could be decreased, and thus obtain the warmer light.

2.5 Potential applications in DSSC

Finally, we also studied the effect of Eu/Y-BTC at different calcination temperatures on photoelectric properties. Figure S9(a) presents the photocurrent–voltage (J–V) curves of solar cells based on P25, P25+Eu/Y-BTC, P25+Y_2O_3:Eu^{3+}/(Eu/Y-BTC), and P25+Y_2O_3:Eu^{3+} and the corresponding photovoltaic parameters are summarized in Table S2 in the ESM. The results indicate that the photoelectric conversion efficiency of P25+Eu/Y-BTC composite cells is not only higher than that of pure TiO_2 cells but also higher than that of other composite cells containing Eu/Y-BTC. This is mainly due to the increase in the amount of dye adsorbed by the photoanode. Figure S9(b) in the ESM presents the UV–vis absorption spectra of desorption dye from N719-sensitized P25 and P25+Eu/Y-BTC sintered at different temperatures photoanodes. We can see that the intensity of the absorption peak at around 500 nm of the dye desorbed from the P25+Eu/Y-BTC photoanode is the strongest. According to the Beer-Lambert law, the amount of dyes desorbed from the P25+Eu/Y-BTC photoanode is 46.6% higher than that of pure P25 photoanode. This is attributed to the introduction of Eu/Y-BTC, which increases the total specific surface area of the photoanode film. Due to the large size of Eu/Y-BTC and Eu/Y-BTC (400 °C), when they are doped in P25, the film quality of the photoanode is negatively affected, and the adsorption capacity of the dye is weakened. The increase in the amount of dye adsorption facilitates the capture of light, thereby improving the photoelectric conversion efficiency of the solar cell. When the Eu/Y-BTC was calcined at 500 °C, the sample almost completely lost its skeleton structure, and the formed Y_2O_3:Eu^{3+} would agglomerate, which affected the adsorption of dyes to a certain extent. Impedance measurements were performed to study the charge transport properties of the P25, P25+Eu/Y-BTC, P25+Y_2O_3:Eu^{3+}/(Eu/Y-BTC), and P25+Y_2O_3:Eu^{3+} thin films. The measurements were conducted before dye adsorption and without the illumination. The largest impedance was obtained from P25+Eu/Y-BTC as shown in Fig. S9(c) in the ESM. It is well known that the larger size of samples can affects the quality of the film. Thus the largest impedance is attributed to the larger size of Eu/Y-BTC without calcination. The size of Eu/Y-BTC decreases with increasing the calcination temperature, which leads to gradually increased film quality, and results in the decrease of impedance. Additionally, the reduction of impedance can be attributed to the formation of channelized transition pathways. The Mott-Schottky plots of P25, P25+Eu/Y-BTC, P25+Y_2O_3:Eu^{3+}/(Eu/Y-BTC), and P25+Y_2O_3:Eu^{3+} films shown in Fig. S9(d) in the ESM indicate that they are n-type semiconductors. Partially enlarged the MS plots of P25 and P25+Y_2O_3:Eu^{3+}/(Eu/Y-BTC) films, we marked the intercept of the X-axis and got the flat band potential in Fig. S9(e) in the ESM. Figure S10 in the ESM shows the incident photon to current (IPCE) spectra of the cells. In addition, the energy level formed by Y_2O_3:Eu^{3+}/(Eu/Y-BTC) makes the photo-generated electrons easier to be transported from dye to TiO_2 instead of recombining with holes in the valence band, which leads to effective electron-hole separation.

3 Conclusions

We have successfully designed and implemented a new

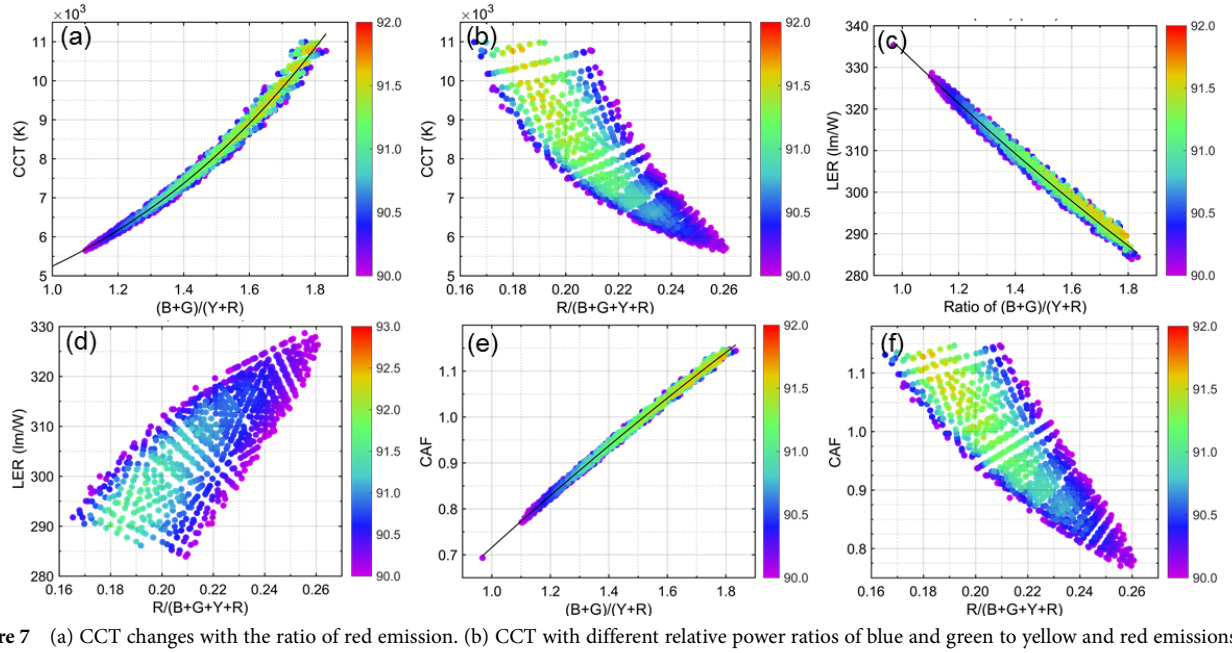

Figure 7 (a) CCT changes with the ratio of red emission. (b) CCT with different relative power ratios of blue and green to yellow and red emissions. (c) The LER changes with the increase in the ratio of red emission. (d) LER as a function of ratios of blue and green emissions to yellow and red emissions. (e) CAF changes with power ratios of red emission. (f) CAF as a function of ratios of the sum of blue and green emissions to the sum of yellow and red emissions. The color bar indicates the CRI with corresponding CCT.

$Y_2O_3:Eu^{3+}$/Eu/Y-BTC host-guest luminous material system based on the confinement effect and antenna effect, where Eu/Y-BTC was prepared by the solvothermal method under moderate conditions first, and then the transformation of Eu/Y-BTC into $Y_2O_3:Eu^{3+}$/Eu/Y-BTC and $Y_2O_3:Eu^{3+}$ was achieved by calcination of Eu/Y-BTC at different temperatures. The morphology of the sample gradually changed with increasing the calcination temperature. The microrod-shaped Eu/Y-BTC changed into $Y_2O_3:Eu^{3+}$/(Eu/Y-BTC) composites with intermediate pores, and then the frame was completely collapsed and $Y_2O_3:Eu^{3+}$ nanoparticles were obtained. A series of test results proved the confinement effects and lattice distortion of ultrasmall $Y_2O_3:Eu^{3+}$ nanocrystals inside Eu/Y-BTC.

The luminescence intensity of $Y_2O_3:Eu^{3+}$/Eu/Y-BTC is higher than those of $Y_2O_3:Eu^{3+}$, which is also reflected in decreased values of Ω_2 from 4.49×10^{-20} cm^2 for $Y_2O_3:Eu^{3+}$/Eu/Y-BTC to 1.14×10^{-20} cm^2 for $Y_2O_3:Eu^{3+}$. Compared with conventional $Y_2O_3:Eu^{3+}$, the total absorption band of Eu/Y-BTC and $Y_2O_3:Eu^{3+}$/(Eu/Y-BTC) composites was significantly red-shifted, indicating these materials can absorb near-UV light emitted from III-nitride LEDs and emit red light. Thus, this type of material has the potential to be used in white LEDs to obtain high efficient white light emission. We have achieved excellent color quality (CRI>90) and extremely high vision performance of white light (an LER of 335 lm/W) by using $Y_2O_3:Eu^{3+}$/(Eu/Y-BTC) composites as the red component in white LEDs. In addition, the large specific surface area of frame materials obtained in this work could also increase the adsorption of dye and improve the light-trapping ability in DSSCs. More importantly, the conduction band minimum of $Y_2O_3:Eu^{3+}$/(Eu/Y-BTC) is in-between that of TiO_2 and Dye, which makes the electron transfer from Dye to TiO_2 much easier. Our results show that by compounding $Y_2O_3:Eu^{3+}$/(Eu/Y-BTC) composites with TiO_2, the DSSC device performance has been improved. Our findings might lead to transformational applications of $Y_2O_3:Eu^{3+}$ in solid-state lighting and photovoltaic technology.

Acknowledgements

This work was supported by the National Natural Science Foundation of China (No. 21871079) and the National Science Foundation (No. 1945558).

Electronic Supplementary Material: Supplementary material (experimental section, Molecular structure, TEM, XPS measurements, excitation and emission spectra, BET and the performance testing of cell) is available in the online version of this article at https://doi.org/10.1007/s12274-020-3104-2.

References

[1] Wang, G. F.; Peng, Q.; Li, Y. D. Lanthanide-doped nanocrystals: Synthesis, optical-magnetic properties, and applications. *Acc. Chem. Res*. **2011**, *44*, 322–332.

[2] Dong, H.; Du, S. R.; Zheng, X. Y.; Lyu, G. M.; Sun, L. D.; Li, L. D.; Zhang, P. Z.; Zhang, C.; Yan, C. H. Lanthanide nanoparticles: From design toward bioimaging and therapy. *Chem. Rev.* **2015**, *115*, 10725–10815.

[3] Xu, J.; Chen, X. Y.; Xu, Y. S.; Du, Y. P.; Yan, C. H. Ultrathin 2D rare-earth nanomaterials: Compositions, syntheses, and applications. *Adv. Mater*. **2020**, *32*, 1806461.

[4] Zhang, X.; Liu, W.; Wei, G. Z.; Banerjee, D.; Hu, Z. C.; Li, J. Systematic approach in designing rare-earth-free hybrid semiconductor phosphors for general lighting applications. *J. Am. Chem. Soc.* **2014**, *136*, 14230–14236.

[5] Phung, N.; Félix, R.; Meggiolaro, D.; Al-Ashouri, A.; Sousa e Silva, G.; Hartmann, C.; Hidalgo, J.; Köbler, H.; Mosconi, E.; Lai, B. et al. The doping mechanism of halide perovskite unveiled by alkaline earth metals. *J. Am. Chem. Soc.* **2020**, *142*, 2364–2374.

[6] Chen, C.; Li, H.; Jin, J. J.; Chen, X.; Cheng, Y.; Zheng, Y.; Liu, D. L.; Xu, L.; Song, H. W.; Dai, Q. L. Long-lasting nanophosphors applied to UV-resistant and energy storage perovskite solar cells. *Adv. Energy Mater.* **2017**, *7*, 1700758.

[7] Zhou, J.; Liu, Q.; Feng, W.; Sun, Y.; Li, F. Y. Upconversion luminescent materials: Advances and applications. *Chem. Rev.* **2015**, *115*, 395–465.

[8] Pan, E.; Bai, G. X.; Ma, B. R.; Lei, L.; Huang, L. H.; Xu, S. Q. Reversible enhanced upconversion luminescence by thermal and electric fields in lanthanide ions doped ferroelectric nanocomposites. *Sci. China Mater*. **2020**, *63*, 110–121.

[9] Zhong, Y. T.; Dai, H. J. A mini-review on rare-earth down-conversion nanoparticles for NIR-II imaging of biological systems. *Nano Res*. **2020**, *13*, 1281–1294.

[10] Li, L.; Tsung, C. K.; Yang, Z.; Stucky, G. D.; Sun, L. D.; Wang, J. F.; Yan, C. H. Rare-earth-doped nanocrystalline titania microspheres emitting luminescence via energy transfer. *Adv. Mater*. **2008**, *20*, 903–908.

[11] Wang, L. Y.; Yan, R. X.; Huo, Z. Y.; Wang, L.; Zeng, J. H.; Bao, J.; Wang, X.; Peng, Q.; Li, Y. D. Fluorescence resonant energy transfer biosensor based on upconversion-luminescent nanoparticles. *Angew. Chem., Int. Ed*. **2005**, *44*, 6054–6057.

[12] Xu, Y. S.; Zeng, Z. C.; Zhang, D.; Liu, S. T.; Wang, X.; Li, S.; Cheng, C. Y.; Wang, J. X.; Liu, Y. Y.; De, G. J. H. et al. Upconversion lifetime imaging of highly-crystalline Gd-based fluoride nanocrystals featuring strong luminescence resulting from multiple luminescent centers. *Adv. Opt. Mater*. **2020**, *8*, 1901495.

[13] Ji, Y. N.; Xu, W.; Li, D. Y.; Zhou, D. L.; Chen, X.; Ding, N.; Li, J.; Wang, N.; Bai, X.; Song, H. W. Semiconductor plasmon enhanced monolayer upconversion nanoparticles for high performance narrowband near-infrared photodetection. *Nano Energy* **2019**, *61*, 211–220.

[14] Wang, Y.; Zheng, K. Z.; Song, S. Y.; Fan, D. Y.; Zhang, H. J.; Liu, X. G. Remote manipulation of upconversion luminescence. *Chem. Soc. Rev*. **2018**, *47*, 6473–6485.

[15] Ji, S. F.; Qu, Y.; Wang, T.; Chen, Y. J.; Wang, G. F.; Li, X.; Dong, J. C.; Chen, Q. Y.; Zhang, W. Y.; Zhang, Z. D. et al. Rare-earth single erbium atoms for enhanced photocatalytic CO_2 reduction. *Angew. Chem., Int. Ed*. **2020**, *59*, 10651–10657.

[16] Wang, G. F.; Peng, Q.; Li, Y. D. Upconversion luminescence of monodisperse CaF_2: Yb^{3+}/Er^{3+} nanocrystals. *J. Am. Chem. Soc*. **2009**, *131*, 14200–14201.

[17] Lei, P. P.; An, R.; Yao, S.; Wang Q. S.; Dong, L. L.; Xu, X.; Du, K. M.; Feng, J.; Zhang, H. J. Ultrafast synthesis of novel hexagonal phase $NaBiF_4$ upconversion nanoparticles at room temperature. *Adv. Mater*. **2017**, *29*, 1700505.

[18] Wang, D.; Wang, R. H.; Liu, L. Y.; Qu, Y.; Wang, G. F.; Li, Y. D. Down-shifting luminescence of water soluble $NaYF_4$: Eu^{3+}@Ag core-shell nanocrystals for fluorescence turn-on detection of glucose. *Sci. China Mater*. **2017**, *60*, 68–74.

[19] Wen, S. H.; Zhou, J. J.; Zheng, K. Z.; Bednarkiewicz, A.; Liu, X. G.; Jin, D. Y. Advances in highly doped upconversion nanoparticles. *Nat. Commun*. **2018**, *9*, 2415.

[20] Bai, G. X.; Lyu, Y. X.; Wu, Z. H.; Xu, S. Q.; Hao, J. H. Lanthanide near-infrared emission and energy transfer in layered WS_2/MoS_2 heterostructure. *Sci. China Mater*. **2020**, *63*, 575–581.

[21] Wang, X.; Zhuang, J.; Peng, Q.; Li, Y. D. A general strategy for nanocrystal synthesis. *Nature* **2005**, *437*, 121–124.

[22] Zhang, L. T.; Kang, W. M.; Ma, Q.; Xie, Y. F.; Jia, Y. L.; Deng, N. P.; Zhang, Y. Z.; Ju, J.; Cheng, B. W. Two-dimensional acetate-based light lanthanide fluoride nanomaterials (F-Ln, Ln=La, Ce, Pr, and Nd): Morphology, structure, growth mechanism, and stability. *J. Am. Chem. Soc*. **2019**, *141*, 13134–13142.

[23] Sui, J. S.; Yan, J. Y.; Wang, K.; Luo, G. S. Efficient synthesis of lithium rare-earth tetrafluoride nanocrystals via a continuous flow method. *Nano Res*. **2020**, *13*, 2837–2846.

[24] Kaiser, M.; Würth, C.; Kraft, M.; Soukka, T.; Resch-Genger, U. Explaining the influence of dopant concentration and excitation power density on the luminescence and brightness of β-$NaYF_4$: Yb^{3+}, Er^{3+} nanoparticles: Measurements and simulations. *Nano Res*. **2019**, *12*, 1871–1879.

[25] Cheng, W.; Rechberger, F.; Niederberger, M. Three-dimensional assembly of yttrium oxide nanosheets into luminescent aerogel monoliths with outstanding adsorption properties. *ACS Nano* **2016**, *10*, 2467–2475.
[26] Xiao, J. D.; Han, L. L.; Luo, J.; Yu, S. H.; Jiang, H. L. Integration of plasmonic effects and schottky junctions into metal-organic framework composites: Steering charge flow for enhanced visible-light photocatalysis. *Angew. Chem., Int. Ed.* **2018**, *57*, 1103–1107.
[27] Ma, X.; Wang, L.; Zhang, Q.; Jiang, H. L. Switching on the photocatalysis of metal-organic frameworks by engineering structural defects. *Angew. Chem.* **2019**, *131*, 12303–12307.
[28] Qin, J. S.; Du, D. Y.; Guan, W.; Bo, X. J.; Li, Y. F.; Guo, L. P.; Su, Z. M.; Wang, Y. Y.; Lan, Y. Q.; Zhou, H. C. Ultrastable polymolybdate-based metal-organic frameworks as highly active electrocatalysts for hydrogen generation from water. *J. Am. Chem. Soc.* **2015**, *137*, 7169–7177.
[29] Chen, W. X.; Pei, J. J.; He, C. T.; Wan, J. W.; Ren, H. L.; Wang, Y.; Dong, J. C.; Wu, K. L.; Cheong, W. C.; Mao, J. J. et al. Single tungsten atoms supported on mof-derived n-doped carbon for robust electrochemical hydrogen evolution. *Adv. Mater.* **2018**, *30*, 1800396.
[30] Jiang, R.; Liu, T. X.; Wu, R. J.; Guo, C.; Chen, Y. G.; Xiang, G. L.; Wang, L. Y. Tailoring N-coordination environment by ligand competitive thermolysis strategy for efficient oxygen reduction. *ACS Appl. Mater. Interfaces* **2020**, *12*, 7270–7276.
[31] Hu, G. F.; Shang, L.; Sheng, T.; Chen, Y. G.; Wang, L. Y. PtCo@NCs with short heteroatom active site distance for enhanced catalytic properties. *Adv. Funct. Mater.* **2020**, *30*, 2002281.
[32] Sun, T. T.; Xu, L. B.; Wang, D. S.; Li, Y. D. Metal organic frameworks derived single atom catalysts for electrocatalytic energy conversion. *Nano Res.* **2019**, *12*, 2067–2080.
[33] Sun, T. T.; Li, Y. L.; Cui, T. T.; Xu, L. B.; Wang, Y. G.; Chen, W. X.; Zhang, P. P.; Zheng, T. Y.; Fu, X. Z.; Zhang, S. L. et al. Engineering of coordination environment and multiscale structure in single-site copper catalyst for superior electrocatalytic oxygen reduction. *Nano Lett.* **2020**, *8*, 6206–6214.
[34] Yang, J.; Li, W.; Wang, D.; Li, Y. D. Electronic metal-support interactions of single-atom and applications in electrocatalysis. *Adv. Mater.*, in press, DOI: 10.1002/adma.202003300.
[35] Li, X. Y.; Rong, H. P.; Zhang, J. T.; Wang, D. S.; Li, Y. D. Modulating the local coordination environment of single-atom catalysts for enhanced catalytic performance. *Nano Res.* **2020**, *13*, 1842–1855.
[36] Nagarkar, S. S.; Joarder, B.; Chaudhari, A. K.; Mukherjee, S.; Ghosh, S. K. Highly selective detection of nitro explosives by a luminescent metal-organic framework. *Angew. Chem., Int. Ed.* **2013**, *52*, 2881–2885.
[37] Lan, A. J.; Li, K. H.; Wu, H. H.; Olson, D. H.; Emge, T. J.; Ki, W.; Hong, M. C.; Li, J. A luminescent microporous metal-organic framework for the fast and reversible detection of high explosives. *Angew. Chem., Int. Ed.* **2009**, *48*, 2334–2338.
[38] He, J.; Xu, J. L.; Yin, J. C.; Li, N.; Bu, X. H. Recent advances in luminescent metal-organic frameworks for chemical sensors. *Sci. China Mater.* **2019**, *62*, 1655–1678.
[39] Stavila, V.; Talin, A. A.; Allendorf, M. D. MOF-based electronic and opto-electronic devices. *Chem. Soc. Rev.* **2014**, *43*, 5994–6010.
[40] Haldar, R.; Wöll, C. Hierarchical assemblies of molecular frameworks—MOF-on-MOF epitaxial heterostructures. *Nano Res.*, in press, DOI: 10.1007/s12274-020-2953-z.
[41] Zhao, B.; Chen, X. Y.; Cheng, P.; Liao, D. Z.; Yan, S. P.; Jiang, Z. H. Coordination polymers containing 1D Channels as selective luminescent probes. *J. Am. Chem. Soc.* **2004**, *126*, 15394−15395.
[42] Xu, X. Y.; Lian, X.; Hao, J. N.; Zhang, C.; Yan, B. A double-stimuli-responsive fluorescent center for monitoring of food spoilage based on dye covalently modified EuMOFs: From sensory hydrogels to logic devices. *Adv. Mater.* **2017**, *29*, 1702298.
[43] Karmakar, A.; Samanta, P.; Desai, A. V.; Ghosh, S. K. Guest-responsive metal-organic frameworks as scaffolds for separation and sensing applications. *Acc. Chem. Res.* **2017**, *50*, 2457–2469.
[44] Yan, B. Lanthanide-functionalized metal-organic framework hybrid systems to create multiple luminescent centers for chemical sensing. *Acc. Chem. Res.* **2017**, *50*, 2789−2798.
[45] Heine, J.; Müller-Buschbaum, K. Engineering metal-based luminescence in coordination polymers and metal-organic frameworks. *Chem. Soc. Rev.* **2013**, *42*, 9232−9242.
[46] Zhang, J.; Liu, F.; Gan, J. L.; Cui, Y. J.; Li, B.; Yang, Y.; Qian, G. D. Metal-organic framework film for fluorescence turn-on H_2S gas sensing and anti-counterfeiting patterns. *Sci. China Mater.* **2019**, *62*, 1445–1453.
[47] Wang, Y.; Gawryszewska-Wilczynsk, P.; Zhang, X. R.; Yin, J.; Wen, Y. Q.; Li, H. R. Photovoltaic efficiency enhancement of polycrystalline silicon solar cells by a highly stable luminescent film. *Sci. China Mater.* **2020**, *63*, 544–551.
[48] Guo, W. X.; Sun, W. W.; Lv, L. P.; Kong, S. F.; Wang, Y. Microwave-assisted morphology evolution of Fe-based metal-organic frameworks and their derived Fe_2O_3 nanostructures for li-ion storage. *ACS Nano* **2017**, *11*, 4198–4205.
[49] Li, Y. S.; Bux, H.; Feldhoff, A.; Li, G. L.; Yang, W. S.; Caro, J. Controllable synthesis of metal-organic frameworks: From MOF nanorods to oriented MOF membranes. *Adv. Mater.* **2010**, *22*, 3322–3326.
[50] Skorupskii, G.; Dincă, M. Electrical conductivity in a porous, cubic rare-earth catecholate. *J. Am. Chem. Soc.* **2020**, *142*, 6920–6924.
[51] Li, W. D.; Ma, P.; Chen, F. F.; Xu, R.; Cheng, Z. H.; Yin, X.; Lin, Y.; Wang, L. Y. $CoSe_2$/porous carbon shell composites as high-performance catalysts toward tri-iodide reduction in dye-sensitized solar cells. *Inorg. Chem. Front.* **2019**, *6*, 2550–2557.
[52] Hao, C. L.; Wu, X. L.; Sun, M. Z.; Zhang, H. Y.; Yuan, A. M.; Xu, L. G.; Xu, C. L.; Kuang, H. Chiral core-shell upconversion nanoparticle@MOF nanoassemblies for quantification and bioimaging of reactive oxygen species *in vivo*. *J. Am. Chem. Soc.* **2019**, *141*, 19373–19378.
[53] Jeong, Y. C.; Seo, J. W.; Kim, J. H.; Nam, S.; Shin, M. C.; Cho, Y. S.; Byeon, J. S.; Park, C. R.; Yang, S. J. Function-regeneration of non-porous hydrolyzed-MOF-derived materials. *Nano Res.* **2019**, *12*, 1921–1930.
[54] Gautier, R.; Li, X. Y.; Xia, Z. G.; Massuyeau, F. Two-step design of a single-doped white phosphor with high color rendering. *J. Am. Chem. Soc.* **2017**, *139*, 1436–1439.
[55] Chen, F.; Wang, Y. M.; Guo, W. W.; Yin, X. B. Color-tunable lanthanide metal-organic framework gels. *Chem. Sci.* **2019**, *10*, 1644–1650.
[56] Shao, B. Q.; Huo, J. S.; You, H. P. Prevailing strategies to tune emission color of lanthanide-activated phosphors for WLED applications. *Adv. Opt. Mater.* **2019**, *7*, 1900319.
[57] Yang, H.; Bright, J.; Kasani, S.; Zheng, P.; Musho, T.; Chen, B. L.; Huang, L.; Wu, N. Q. Metal–organic framework coated titanium dioxide nanorod array P–N heterojunction photoanode for solar water-splitting. *Nano Res.* **2019**, *12*, 643–650.
[58] Chen, B.; Yang, Y.; Zapata, F.; Lin, G.; Qian, G.; Lobkovsky, E. B. Luminescent open metal sites within a metal-organic framework for sensing small molecules. *Adv. Mater.* **2007**, *19*, 1693–1696.
[59] Cai, Y. J.; Li, X. Y.; Wu, K. B.; Yang, X. F. Electrochemical sensing performance of Eu-BTC and Er-BTC frameworks toward sunset yellow. *Anal. Chim. Acta* **2019**, *1062*, 78–86.
[60] Cornil, J.; Beljonne, D.; Calbert, J. P.; Brédas, J. L. Interchain interactions in organic π-conjugated materials: Impact on electronic structure, optical response, and charge transport. *Adv. Mater.* **2001**, *13*, 1053–1067.